A Massive, Clumpy Molecular Gas Distribution and Displaced AGN in Zw 3146

A. N. Vantyghem[1] , B. R. McNamara[2,3,4] , C. P. O'Dea[1] , S. A. Baum[1], F. Combes[5,6] , A. C. Edge[7] , A. C. Fabian[8] ,
M. McDonald[9] , P. E. J. Nulsen[9,10] , H. R. Russell[8], and P. Salomé[5]

[1] University of Manitoba, Department of Physics and Astronomy, Winnipeg, MB R3T 2N2, Canada; Adrian.Vantyghem@umanitoba.ca
[2] Department of Physics and Astronomy, University of Waterloo, Waterloo, ON N2L 3G1, Canada
[3] Waterloo Centre for Astrophysics, Waterloo, ON N2L 3G1, Canada
[4] Perimeter Institute for Theoretical Physics, Waterloo, Canada
[5] LERMA, Observatoire de Paris, PSL University, CNRS, Sorbonne University Paris, France
[6] Collège de France, 11 place Marcelin Berthelot, 75005 Paris, France
[7] Department of Physics, Durham University, Durham DH1 3LE, UK
[8] Cambridge University, Institute of Astronomy, Madingley Road, Cambridge CB3 0HA, UK
[9] Harvard-Smithsonian Center for Astrophysics, 60 Garden Street, Cambridge, MA 02138, USA
[10] ICRAR, University of Western Australia, 35 Stirling Highway, Crawley, WA 6009, Australia

Abstract

We present a recent Atacama Large Millimeter/submillimeter Array observation of the $CO(1-0)$ line emission in the central galaxy of the Zw 3146 galaxy cluster ($z = 0.2906$). We also present updated X-ray cavity measurements from archival Chandra observations. The $5 \times 10^{10} M_\odot$ supply of molecular gas, which is confined to the central 4 kpc, is marginally resolved into three extensions that are reminiscent of the filaments observed in similar systems. No velocity structure that would be indicative of ordered motion is observed. The three molecular extensions all trail X-ray cavities, and are potentially formed from the condensation of intracluster gas lifted in the wakes of the rising bubbles. Many cycles of feedback would be required to account for the entire molecular gas reservoir. The molecular gas and continuum source are mutually offset by 2.6 kpc, with no detected line emission coincident with the continuum source. It is the molecular gas, not the continuum source, that lies at the gravitational center of the brightest cluster galaxy. As the brightest cluster galaxy contains possible tidal features, the displaced continuum source may correspond to the nucleus of a merging galaxy. We also discuss the possibility that a gravitational wave recoil following a black hole merger may account for the displacement.

1. Introduction

Galaxy clusters are permeated by a hot (10^7–10^8 K), diffuse intracluster medium (ICM) that shines brightly in X-rays. In cool core galaxy clusters the central density is sharply peaked at the position of the brightest cluster galaxy (BCG). The correspondingly high X-ray luminosity in the cluster core should result in the ICM condensing into clouds of cold, molecular gas and forming stars at rates of hundreds to thousands of solar masses per year (Fabian 1994; Peterson & Fabian 2006). Indeed, the BCGs in cool core clusters are the largest and most luminous elliptical galaxies in the universe. They burgeon with star formation proceeding at rates of ~ 1–$500 M_\odot$ yr^{-1} (e.g., McNamara 2004; O'Dea et al. 2008; McDonald et al. 2011; Donahue et al. 2015; Tremblay et al. 2015; McDonald et al. 2018), host luminous emission-line nebulae (e.g., Lynds 1970; Heckman 1981; Cowie et al. 1983; Hu et al. 1985; Crawford et al. 1999), and harbor molecular gas reservoirs more massive than even gas-rich spiral galaxies, sometimes exceeding $10^{10} M_\odot$ (Edge 2001; Edge et al. 2002; Edge & Frayer 2003; Salomé & Combes 2003). These signatures of gas condensation are prevalent in systems whose central cooling times fall below a sharp threshold of 1 Gyr (Cavagnolo et al. 2008; Rafferty et al. 2008; Pulido et al. 2018). Nevertheless, they account for less than 10% of what would be expected from an unimpeded cooling flow.

Active galactic nuclei (AGN) feedback regulates the rate of ICM cooling (for reviews, see McNamara & Nulsen 2007, 2012; Fabian 2012). The "radio-mode" of AGN feedback is nearly ubiquitous in giant ellipticals and galaxy clusters with short central cooling times (Burns 1990; Dunn & Fabian 2006; Best et al. 2007; Bîrzan et al. 2012). Radio jets launched by the central AGN inflate bubbles, drive shock fronts, and generate sound waves in the hot atmosphere (e.g., McNamara et al. 2000; Churazov et al. 2000, 2001; Blanton et al. 2001; Fabian et al. 2006). The sizes and surrounding pressures of radio bubbles, which manifest as cavities in the X-ray surface brightness, are used in a direct estimate of the AGN power output. In a large sample of objects, the AGN power output closely matches the radiative losses from the surrounding ICM (Bîrzan et al. 2004; Dunn & Fabian 2006; Rafferty et al. 2006; Nulsen et al. 2009). This, along with the preponderance of systems with central cooling times of < 1 Gyr, implies that AGN heating and radiative cooling are coupled in a long-lived feedback loop.

In order to establish and maintain such a feedback loop, radiative losses in the ICM must be tied to accretion onto the central supermassive black hole (SMBH). Molecular gas is the most likely intermediary. Overdensities in the ICM, generated by turbulence or AGN feedback, rapidly condense into a multiphase atmosphere that is dominated by molecular gas (e.g., Sharma et al. 2012; McCourt et al. 2012; Gaspari et al. 2013, 2017; Li & Bryan 2014; Voit 2018). Ram pressure and collisions between cold clouds are both effective mechanisms for driving cold clouds toward the galactic center (Pizzolato & Soker 2005, 2010). This results in "chaotic cold accretion" (Gaspari et al. 2013), where the stochastic production of cold

clouds feeds black hole growth and regulates the feedback loop between ICM cooling and AGN heating.

Though molecular gas is the fuel for AGN feedback, its distribution is also shaped by the AGN. Radio jets drive fast outflows of ionized, neutral, and molecular gas on parsec to kiloparsec scales (e.g., Morganti et al. 2005, 2013; Nesvadba et al. 2006; Alatalo et al. 2011; Dasyra & Combes 2011; Sturm et al. 2011; Tadhunter et al. 2014; Morganti et al. 2015). A gentler coupling between AGN feedback and molecular gas is observed in BCGs (Olivares et al. 2019; Russell et al. 2019). The rotationally supported disks that would be expected from the long-lived accumulation of molecular clouds in the galactic center are rare (Hamer et al. 2014; Russell et al. 2019). Instead, billions of solar masses of cold gas are situated in kiloparsec-scale filaments that trail X-ray cavities (e.g., Salomé et al. 2006, 2008; Lim & Ao 2008; Lim et al. 2012; McDonald et al. 2012a; McNamara et al. 2014; Russell et al. 2014, 2016, 2017a, 2017b; Vantyghem et al. 2016, 2018, 2019). The detection of redshifted absorption lines indicates that some of this gas rains back onto the central galaxy in a circulation flow (David et al. 2014; Tremblay et al. 2016, 2018; Rose et al. 2019b, 2019a, 2020).

Motivated by these observations, McNamara et al. (2016) proposed the "stimulated feedback" paradigm (see also Revaz et al. 2008). As radio bubbles rise buoyantly, they uplift low-entropy ICM gas from the cluster core to an altitude where it becomes thermally unstable. The cold clouds decouple from the radio bubbles and fall back onto the central galaxy as in chaotic cold accretion. In this way, AGN feedback stimulates the production of its own fuel.

Mapping the spatial distribution of cold gas in BCGs in all but the closest and most gas-rich systems has only become possible with the arrival of the Atacama Large Millimeter/submillimeter Array (ALMA). Here we present a new ALMA observation targeting the $CO(1-0)$ emission line in the BCG of Zw 3146, which is one of the most extreme cool core clusters and brightest CO emitters known. If left unimpeded, its soft (0.1–2.4 keV) X-ray luminosity of 2×10^{45} erg s^{-1} (Ebeling et al. 1998; Böhringer et al. 2000) would lead to a mass deposition rate of $1250\,M_\odot$ yr^{-1} (Edge et al. 1994). Indeed, the BCG in Zw 3146 is exceptionally active, showing a blue continuum and luminous nebular emission lines (Allen et al. 1992; Hicks & Mushotzky 2005), an infrared luminosity of $4 \times 10^{11}\,L_\odot$ (Egami et al. 2006b), an $8 \times 10^{10}\,M_\odot$ reservoir of cold gas (Edge 2001; Edge & Frayer 2003), and strong molecular H$_2$ emission lines from $\sim 10^{10}\,M_\odot$ of warm H$_2$ (Egami et al. 2006a). The infrared luminosity implies a star formation rate of $\sim 70\,M_\odot$ yr^{-1} (Egami et al. 2006b; Edge et al. 2010; Hicks et al. 2010; Hoffer et al. 2012).

Spectroscopic measurements indicate that the true mass deposition rate is much lower than that implied by the X-ray luminosity (e.g., Egami et al. 2006b). Any continuous radiative cooling flow from the bulk temperature at 4 keV to 0.01 keV is less than $50\,M_\odot$ yr^{-1} (Liu et al. in preparation, see also Liu et al. 2019). The rate of gas cooling to 0.7 keV is $130\,M_\odot$ yr^{-1}, with less than $78\,M_\odot$ yr^{-1} cooling to lower temperatures. AGN feedback is likely responsible for the heavily suppressed cooling rate. The X-ray atmosphere hosts several cavities that replenish energetic losses at a rate of $\sim 6 \times 10^{45}$ erg s^{-1} (Rafferty et al. 2006). The combination of a massive reservoir of molecular gas and powerful AGN feedback make Zw 3146 a prime candidate to contain molecular filaments trailing X-ray cavities, as observed in other BCGs.

Throughout this work we assume a standard ΛCDM cosmology with $H_0 = 70$ km s^{-1} Mpc^{-1}, $\Omega_{m,0} = 0.3$, and $\Omega_{\Lambda,0} = 0.7$. At the redshift of Zw 3146 ($z = 0.29007$), the angular scale is $1'' = 4.35$ kpc and the luminosity distance is 1500 Mpc.

2. Observations and Data Reduction

The BCG of the Zw 3146 galaxy cluster (2MASX J10233960 +0411116—R.A.: 10:23:39.6340, decl.: +4:11:10.660) was observed with ALMA in Band 3 (Cycle 4, ID 2016.1.01269.S, PI Vantyghem), centered on the $CO(1-0)$ line at 89.316 GHz. The observations were conducted in three blocks from 2019 August 15 to 19, with a total on-source integration time of 106 minutes. Each observing block was split into ∼6 minute on-source integrations interspersed with observations of the phase calibrator. The 69″.2 primary beam was centered on the BCG nucleus in a single pointing common to each observing block. A total of 41–44 antennas were used in these observations, with baselines ranging from 41 m to 3637 m. This corresponds to a maximum recoverable scale of 10″. A single spectral window in the frequency division correlator mode was used to study the CO spectral line with 1.875 GHz bandwidth and 488 kHz (1.6 km s^{-1}) frequency resolution, though the data were later smoothed to a coarser velocity grid. An additional three basebands with the time division correlator mode, each with a 2 GHz bandwidth and frequency resolution of 15.625 MHz, were employed in order to measure the continuum source.

The observations were calibrated in CASA version 5.4.0 (McMullin et al. 2007) using the pipeline reduction scripts. Continuum-subtracted data cubes were created using UVCONT-SUB and CLEAN. Additional phase self-calibration was attempted, but the continuum source was too faint to provide an improvement in signal-to-noise ratio. Images of the line emission were reconstructed using Briggs weighting with a robust parameter of 0.5. The final $CO(1-0)$ data cube had a synthesized beam of 0″.30 × 0″.26 (P.A. −79°.5) and was binned to a velocity resolution of 20 km s^{-1}. The rms noise in line-free channels was 2.4 mJy beam^{-1}.

2.1. Systemic Velocity

The gas velocities presented in this work are measured in the molecular gas rest frame. This was determined by extracting a spectrum from a $3'' \times 3''$ region that encompasses all of the observed line emission, as shown in Figure 1. A single Gaussian fitted to the spectrum yields a molecular gas redshift of 0.29007 ± 0.00003. This is consistent with the $CO(1-0)$ velocity centroids measured in previous work (e.g., Edge 2001).

Previous works on Zw 3146 generally adopted a redshift of 0.29060 ± 0.00010, which was determined from the emission-line nebula (Allen et al. 1992). The molecular gas rest frame is blueshifted by 158 ± 30 km s^{-1} from this nebular redshift. The discrepancy may originate from differences in the distribution of gas traced by each observation. The molecular gas is confined to the central few kiloparsecs of the BCG, while nebular emission is present on larger scales.
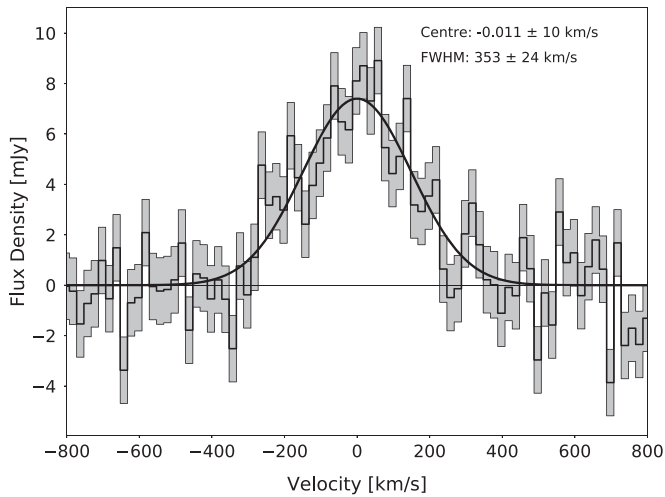
Figure 1. CO(1−0) spectrum extracted from a 13 kpc × 13 kpc (3″ × 3″) box that contains all of the observed emission.

3. Results

3.1. Molecular Gas Mass

The integrated flux ($S_{CO}\Delta v$) of the CO(1−0) line can be converted to molecular gas mass through (Solomon et al. 1987; Solomon & Vanden Bout 2005; Bolatto et al. 2013)

$$M_{mol} = 1.05 \times 10^4 \frac{X_{CO}}{X_{CO,gal}} \left(\frac{S_{CO}\Delta v\, D_L^2}{1 + z} \right) M_\odot, \qquad (1)$$

where z is the redshift of the source, D_L is the luminosity distance in Mpc, and $S_{CO}\Delta v$ is in Jy km s^{-1}. The CO-to-H$_2$ conversion factor, X_{CO}, has been studied extensively in the local universe. Its nominal value is the mean empirically derived Galactic value, $X_{CO,gal} = 2 \times 10^{20}$ cm^{-2} (K km s^{-1})$^{-1}$ (Bolatto et al. 2013).

Lacking an independent calibration of X_{CO} in BCGs, we follow standard practice by adopting the Galactic value throughout this work. The only estimate of X_{CO} in a BCG was obtained recently through the detection of ^{13}CO(3−2) emission in RXJ0821.0+0752 (Vantyghem et al. 2017). As ^{13}CO is an optically thin emission line, it provided a direct measurement of the ^{13}CO column density. In combination with a measurement of CO(1−0) and CO(3–2) line intensities and a number of assumptions, X_{CO} was estimated to be half of the Galactic value. This is reassuringly close to the Galactic value given the significant morphological differences between BCGs and the Milky Way disk. Until a direct calibration in BCGs is available, we continue to follow the standard practice of adopting the Galactic X_{CO}.

The primary reasons for the CO-to-H$_2$ conversion factor to vary between galaxies are the gas metal abundance and excitation conditions. In metal-poor dwarf galaxies X_{CO} is elevated by more than an order of magnitude because CO traces a smaller fraction of the overall H$_2$ distribution (Bolatto et al. 2013). The molecular gas in BCGs likely forms by condensation of the hot atmosphere, which has typical metallicities of ∼0.6–0.8 $Z_\odot$ (e.g., De Grandi & Molendi 2001; De Grandi et al. 2004). The metal abundance of molecular clouds in BCGs is therefore expected to be similar to that of the Milky Way.

X_{CO} is driven downward by factors of ∼5 in starbursts (e.g., Ultra-Luminous Infrared Galaxies; ULIRGs), where the hot, dense molecular gas has an elevated luminosity per unit mass. BCGs also have high star formation rates, approaching $1000\, M_\odot$ yr^{-1} in the most extreme cases (e.g., the Phoenix Cluster; McDonald et al. 2012b). However, the molecular gas in BCGs is often distributed over much larger spatial scales than in ULIRGs, where the gas is confined to the central kiloparsec. Despite their elevated star formation rates (SFRs), BCGs still lie on the Kennicutt–Schmidt relation (Kennicutt 1998; Kennicutt & Evans 2012) alongside normal galaxies (see, e.g., McNamara et al. 2014; Russell et al. 2014; Vantyghem et al. 2018).

The SFR in Zw 3146, $70\, M_\odot$ yr^{-1} (Egami et al. 2006b), is comparable to that of other BCGs for which the Galactic X_{CO} has been adopted. However, Zw 3146 is also the most luminous and distant H$_2$ emitter observed, with a line luminosity of $L[\text{H}_2\, 0{-}0\, S(3)] = 6.1 \times 10^{42}$ erg s^{-1} (Egami et al. 2006b). A cosmic-ray dominated region or excitation through shocks driven by the AGN may be required to explain such strong rotational H$_2$ lines (Ferland et al. 2009; Bayet et al. 2010; Guillard et al. 2012). This could impact the value of X_{CO}. Strong H$_2$ line emission is observed in many cool core clusters (Donahue et al. 2011) and radio galaxies (Ogle et al. 2010).

A spatially integrated CO(1−0) spectrum was extracted from a 13 kpc × 13 kpc (3″ × 3″) box containing all of the detected line emission. The spectrum, shown in Figure 1, is best fit by a single Gaussian with total flux of 2.78 ± 0.17 Jy km s^{-1}. This corresponds to 5.05 ± 0.50 × 10^{10} $M_\odot$ of molecular gas. A list of all fitted parameters is provided in Table 1. No other CO(1−0) line emission was detected throughout the 70″ primary beam of these observations.

Previous single-dish and interferometric radio observations of Zw 3146 with the IRAM-30 m telescope and Owens Valley Radio Telescope (OVRO) yielded CO(1−0) integrated fluxes of 5.2 ± 1.2 Jy km s^{-1} and 5.7 ± 0.9 Jy km s^{-1}, respectively (Edge 2001; Edge & Frayer 2003). Our ALMA observation recovers 50% of this flux; a similar fraction to that of other BCGs (e.g., David et al. 2014; Russell et al. 2014; McNamara et al. 2014; Vantyghem et al. 2018). The line emission in the OVRO observations, which recovers all of the single-dish flux, is unresolved by the 6″.7 × 4″.7 beam. This suggests that our ALMA observations are missing large-scale flux, predominantly on scales of ∼5″ (22 kpc).

3.2. Molecular Gas Distribution and Kinematics

Maps of integrated flux, velocity, and FWHM of the CO(1−0) line were created by fitting the spectra extracted from individual pixels within the data cube. Each spectrum was averaged over a box the size of the synthesized beam. We allowed for the possibility of multiple coincident velocity structures by fitting each spectrum with up to two Gaussian components. The significance of each velocity component was tested using a Monte Carlo analysis employing 10,000 iterations, with a detection requiring 5σ significance. The presence of one component was required before attempting to fit a second. We found that a single Gaussian component was sufficient to accurately model the spectrum for each pixel. Instrumental broadening has been incorporated into the model.

The integrated flux map is presented in the lower left panel of Figure 2, and the velocity centroid and full-width at half maximum (FWHM) maps are presented in Figure 3. The

Table 1
Parameters of Molecular Features

Region	$\chi^2/$ dof	Velocity Center ($km\,s^{-1}$)	FWHM ($km\,s^{-1}$)	Integrated Flux[a] ($Jy\,km\,s^{-1}$)	Gas Mass[a] ($10^8\,M_\odot$)
All Emission	221.2/197	0.0 ± 10	353 ± 24	2.78 ± 0.17	504 ± 30
Central Clump	226.3/197	-59.6 ± 8.2	265 ± 19	0.201 ± 0.013	36.4 ± 2.3
Clump 1	224.0/197	17.2 ± 6.1	177 ± 14	0.289 ± 0.02	52.7 ± 3.7
Clump 2	221.6/197	28 ± 12	288 ± 28	0.429 ± 0.036	78.3 ± 6.7
Clump 3	218.6/197	-69 ± 17	415 ± 41	0.46 ± 0.04	83.7 ± 7.1

Note.
[a] All spectra have been corrected for the response of the primary beam and instrumental broadening.

molecular gas distribution is compact, with all of the detected gas confined to a $1''$ (4.35 kpc) radius. It is marginally resolved into three extensions to the NE, SE, and W. These extensions do not exhibit any clear velocity gradients. The emission is at its most blueshifted ($-150\,km\,s^{-1}$) at the central peak and in the farthest extent of the SE extension. The NE and W extensions have more moderate velocities ($0–50\,km\,s^{-1}$), but the velocity transition to the central value occurs over the span of about a beam, so it is likely the result of the resolution element smearing two distinct velocities together. The line widths, which range from $100\,km\,s^{-1}$ to $400\,km\,s^{-1}$ FWHM, are broader than those seen along filaments in other systems ($< 100\,km\,s^{-1}$; e.g., Russell et al. 2016; Vantyghem et al. 2016, 2018), consistent with a superposition of gas structures at a range of velocities.

Chandra X-ray, HST WFPC2 F606W, Lyα (HST ACS/SBC F140LP), and far-ultraviolet (FUV; HST ACS/SBC F165LP) images (O'Dea et al. 2010; Tremblay et al. 2015) are shown alongside the CO(1−0) total flux map in Figure 2. The box in the X-ray image corresponds to the fields of view for the HST images, while the ALMA field of view is shown in the HST images. The central galaxy contains bright knots of nebular emission and FUV flux from recent star formation, one of which is coincident with the molecular gas. A brighter Lyα and FUV peak is located 3.25 kpc ESE of the molecular gas peak. No molecular gas is present at this position; the CO emission truncates where the Lyα and FUV fluxes begin to increase. Dust attenuation may account for this anticorrelation between the molecular gas and FUV emission. Features that may be indicative of a merger remnant are seen in the HST F606W image. The most prominent clumps and filament are identified in Figure 2. However, this filter also includes Hβ and [O III] line emission, which may account for some of the observed features.

The molecular gas is offset by 1 kpc to the south of the peak in X-ray emission, which itself does not coincide with structure at any other wavelength. The bright X-ray emission in the cluster core arcs around the position of the CO(1−0) peak. In addition, the X-ray atmosphere contains a series of depressions that likely correspond to cavities inflated by the central AGN (see Section 3.5).

The molecular extensions can be better visualized by subtracting the contribution from an unresolved point source coincident with the CO(1−0) peak. This is shown in Figure 4. First, we created an image of the beam centered on the pixel with the largest integrated flux. This image was further convolved with a beam-shaped top-hat kernel, as the pixel-based spectral fitting used to create the maps extracts the emission from a region of this shape. The image was then scaled to match the flux of the brightest pixel and subtracted from the integrated flux map. The unresolved emission subtracted from the integrated flux map amounted to 22% of the total flux.

The resulting map shows that the gas morphology is separated into the three extensions, although none of them are resolved. They have been identified in Figure 4. The corresponding spectra are shown in Figure 5, and their spectral fits are listed in Table 1.

3.3. Millimeter Continuum

An image of the continuum at 96.193 GHz (3.1166 mm) was created by imaging the line-free channels in a square region measuring $40''$ on each side. A single, unresolved source was identified (R.A.: 10:23:39.5948, decl.: +4:11:11.032), which had a total integrated flux density of $133 \pm 13\,\mu Jy$. The contours for this source are shown in red in Figure 2. These contours begin at 3σ, where $\sigma = 7.45\,\mu Jy\,beam^{-1}$, and increase in 4σ steps. A two-dimensional Gaussian fit to the continuum flux yielded an accuracy for the centroid of $0.''006$. We searched for, but did not detect, evidence for absorption against the continuum source using the native velocity resolution of the observations.

In Figure 6 we plot the ALMA continuum alongside flux measurements at lower frequencies, which were obtained from either the Very Large Array (VLA) or BIMA (Egami et al. 2006b; Coble et al. 2007; Giacintucci et al. 2014). Error bars are included, but are smaller than the markers for all measurements except those provided in this work. The spectral energy distribution (SED) is best fit by a power law with spectral index[11] $\alpha = 0.685 \pm 0.063$, which is a typical value for an AGN (e.g., Hogan et al. 2015).

3.4. The Molecular Gas–AGN Offset

As is evident in Figure 2, the molecular gas and continuum source are mutually offset. The two peaks are 2.6 kpc ($0.''6$) apart, and only a minimal overlap is present in the fainter reaches of the two distributions. This offset cannot originate from a phase calibration issue, as the continuum and line measurements are obtained from the same observation.

Independent observations of the radio continuum at lower resolution confirm the position of the millimeter continuum source identified here. In a VLA 4.9 GHz observation, the continuum centroid is $0.''3$ SSW of the ALMA continuum source (O'Dea et al. 2010). Though the coarse resolution ($1.''4 \times 0.''9$) prevents the CO(1−0) centroid and continuum

---

[11] Following the convention $S_\nu \propto \nu^{-\alpha}$.
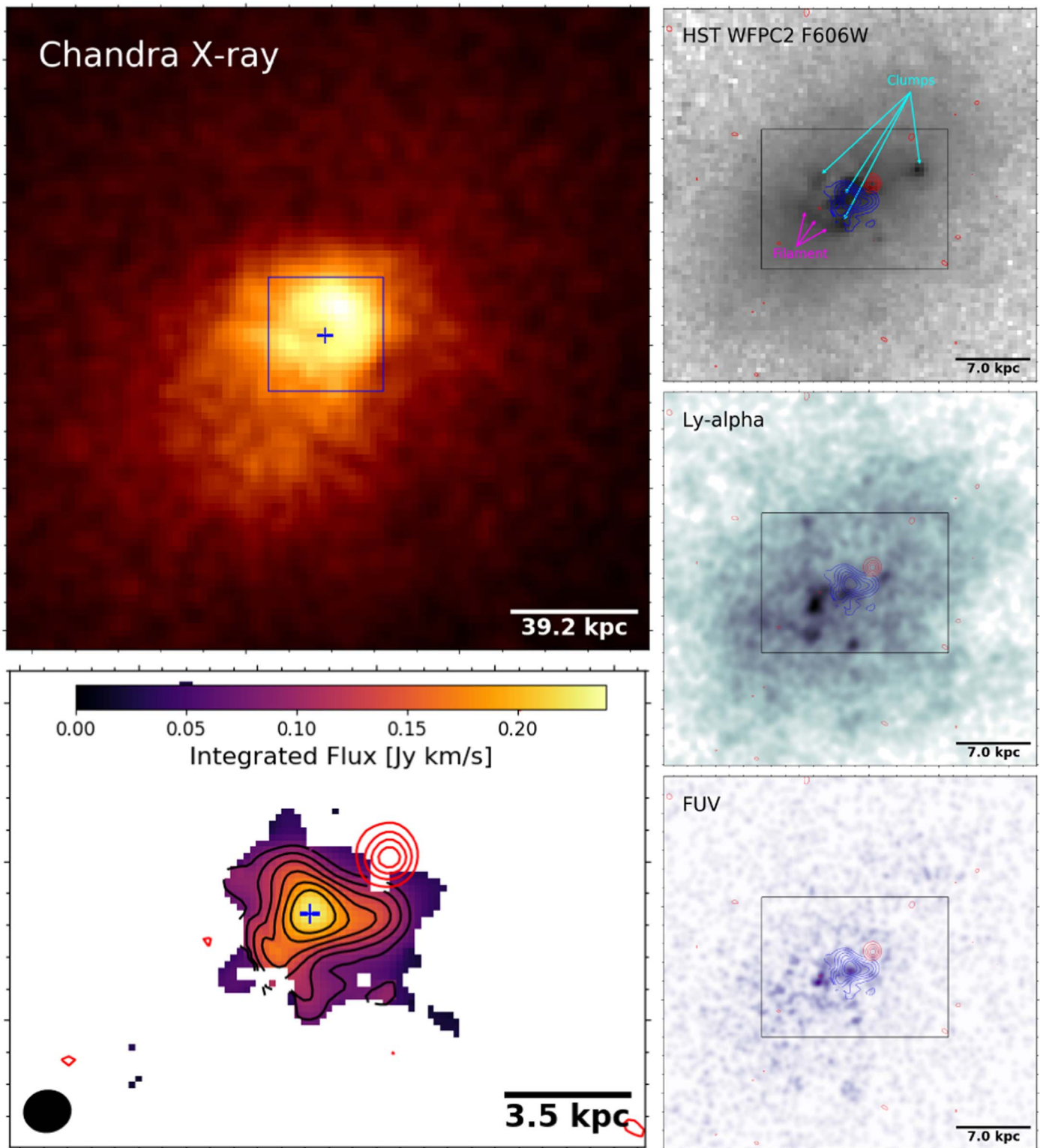
Figure 2. A multiwavelength view of the Zw 3146 cluster. The top-left panel shows the lightly smoothed Chandra X-ray 0.5–7 keV image. The box indicates the field of view for all three images on the right. From top to bottom, these are the HST WFPC2 F606W image, Lyα, and the far-ultraviolet (FUV; Tremblay et al. 2015). The most prominent substructures in the HST F606W image have been identified. Note that the F606W filter includes a contribution from Hβ and [O III] line emission. The rectangle in each of the panels on the right indicate the field of view of the ALMA CO(1−0) image, shown on the bottom left. The solid black ellipse is the synthesized beam. The blue contours and "+" indicate the CO(1−0) emission and its centroid, respectively. The red contours correspond to 4σ steps in the millimeter continuum, beginning at 3σ and with $\sigma = 7.45\ \mu$Jy beam^{-1}.

source from being definitively distinguished, the VLA centroid is closer to the ALMA continuum position. Note that the VLA coordinates were reported in the B1950 equinox, so they have

been converted to J2000. Giacintucci et al. (2014) also report a continuum centroid corresponding to VLA 4.9 GHz and 8.5 GHz observations in the C configuration. The position is
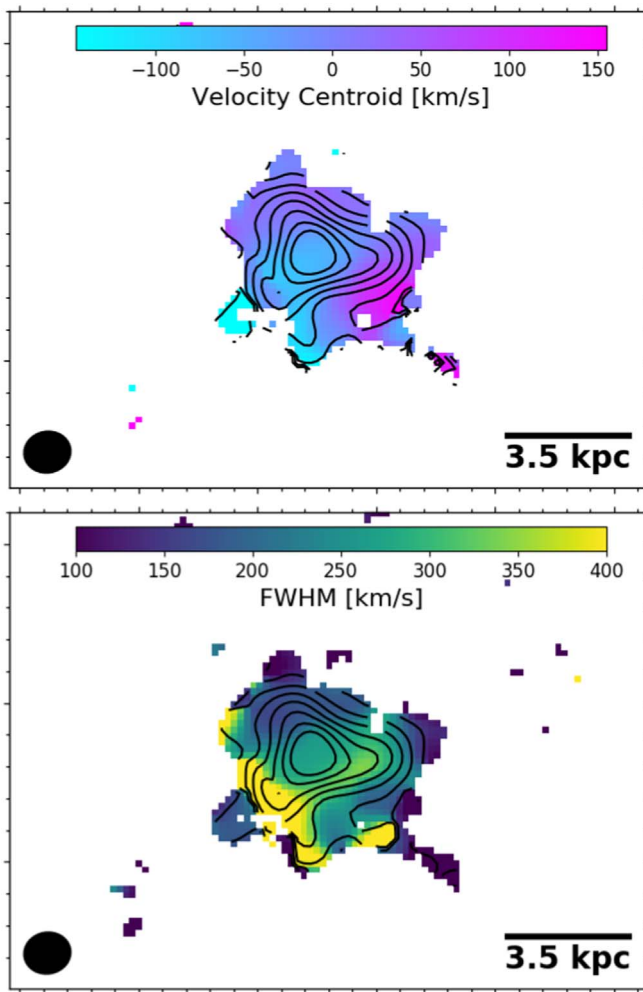
Figure 3. Maps of velocity centroid and line FWHM determined by the pixel-by-pixel fitting scheme discussed in Section 3.2. These images have the same field of view as the CO(1−0) flux map in Figure 2. The solid black ellipse is the synthesized beam.
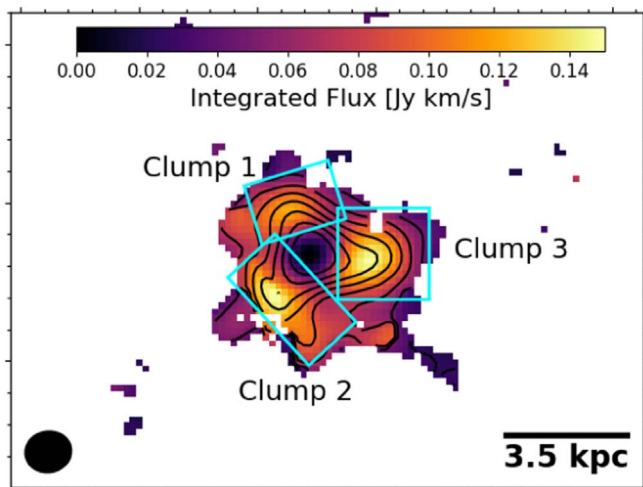
Figure 4. Maps of the integrated CO(1−0) flux after subtracting a point source centered on the peak of the gas distribution. The contours correspond to the original distribution of integrated flux, as shown in Figure 3.
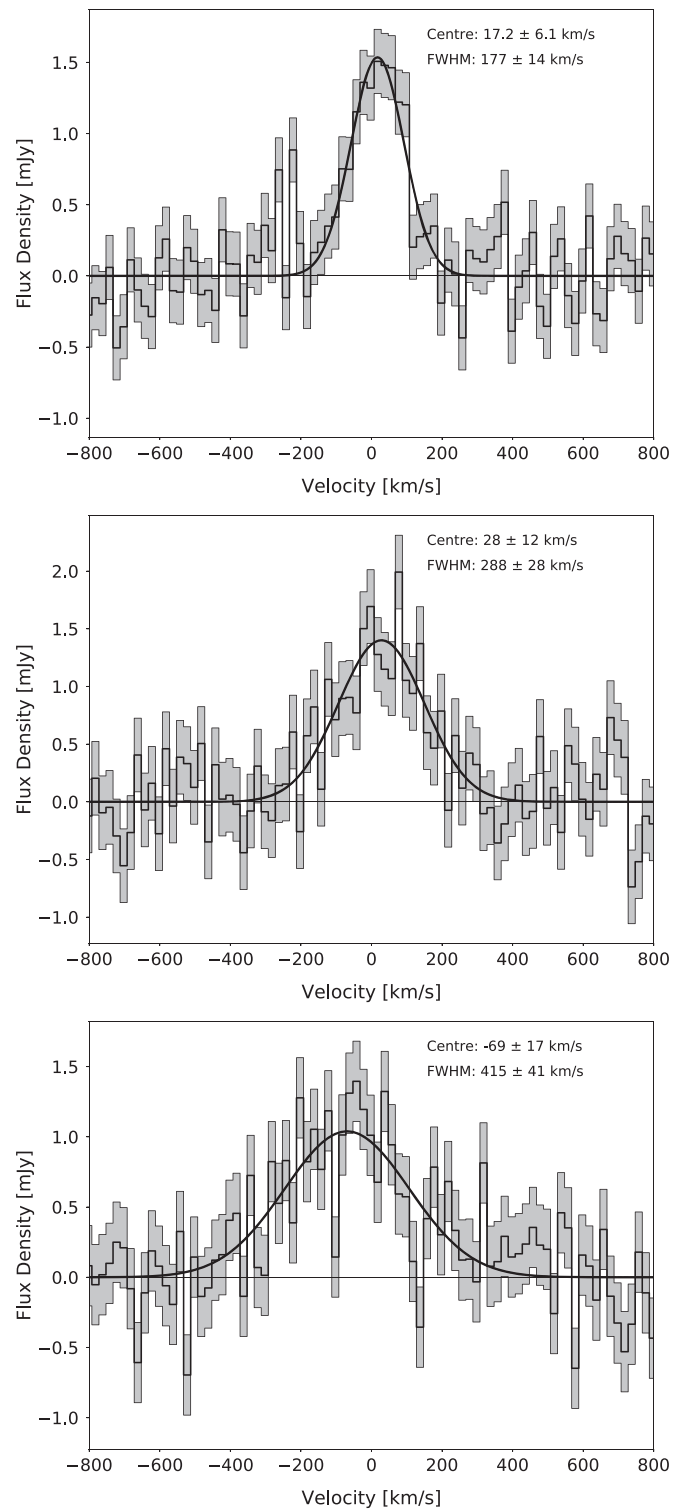
Figure 5. CO(1−0) spectral to the three clumps identified in Figure 4.

consistent with the location of the ALMA continuum source, although no uncertainties are provided and the beam sizes are larger. Nevertheless, these independent radio observations indicate that the ALMA continuum position reported here is likely accurate.

The stellar continuum is difficult to disentangle from nebular emission in the HST images. In order to determine the position

6
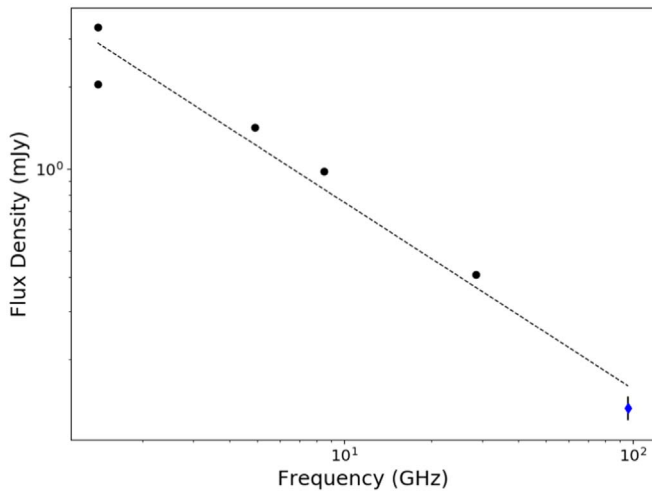
Figure 6. Radio spectral energy distribution, with the ALMA continuum source measurement shown in blue. The best-fitting power law, indicated by the dashed line, has a slope of -0.685 ± 0.063.

Figure 7. DECaLS r-band image of Zw 3146 in the same field of view as the HST F606W image in Figure 2. Contours of the ALMA CO(1−0) emission and continuum source are shown in blue and red, respectively. The black contours correspond to the DECaLS r-band flux. The black rectangle indicates the ALMA CO(1−0) field of view as shown in Figure 2.

Figure 8. X-ray image processed using the GGM algorithm to enhance surface brightness edges, shown with the same field of view as the X-ray image in Figure 2. Six candidate X-ray cavities have been identified. The location of the cluster center is indicated by the black "Y". The blue "+" indicates the molecular gas centroid.

of the galactic center, we obtained a Dark Energy Camera Legacy Survey (DECaLS) r-band image using the legacy skyviewer[12], which is shown in Figure 7. This image is uncontaminated by nebular line emission and stellar features from a merger remnant, providing a smooth tracer of the stellar continuum. Contours of molecular line emission and continuum source are overlaid in blue and red, respectively, in Figure 7, along with black contours tracing the stellar emission. It is the molecular gas that is coincident with the galactic center, not the continuum emission from the AGN.

All taken together, these results imply that the molecular gas resides at the galactic center while the continuum source is offset by 2.6 kpc. The molecular gas is coincident with both the stellar centroid and bright knots of nebular emission and star formation, while the continuum position is consistent with independent measurements at lower frequencies. This correspondence spanning multiple types of observations indicates that the astrometry of the ALMA observation is reliable. We explore possible physical interpretations for this offset in Section 4.1.

3.5. X-Ray Cavities

In order to investigate any possible connection between the molecular gas and X-ray cavities, we present a new search for cavities in Zw 3146 using the Chandra data reduced by Hogan et al. (2017) and Pulido et al. (2018). The 0.5–7 keV X-ray surface brightness image is shown in Figure 2. In addition, we have processed this image using the Gaussian gradient magnitude algorithm (GGM; Sanders et al. 2016a, 2016b) with a radially dependent filtering kernel. This algorithm enhances edges in surface brightness. The resulting image is shown in Figure 8, sharing a field of view with the X-ray image in Figure 2. The X-ray atmosphere contains a series of surface brightness depressions and edges corresponding to X-ray cavities and cold fronts, respectively (Forman et al. 2002; Rafferty et al. 2006).

We manually identified six candidate X-ray cavities using a combination of the GGM filtered image and original X-ray image. The sizes were determined qualitatively by estimating

---

[12] https://www.legacysurvey.org/viewer
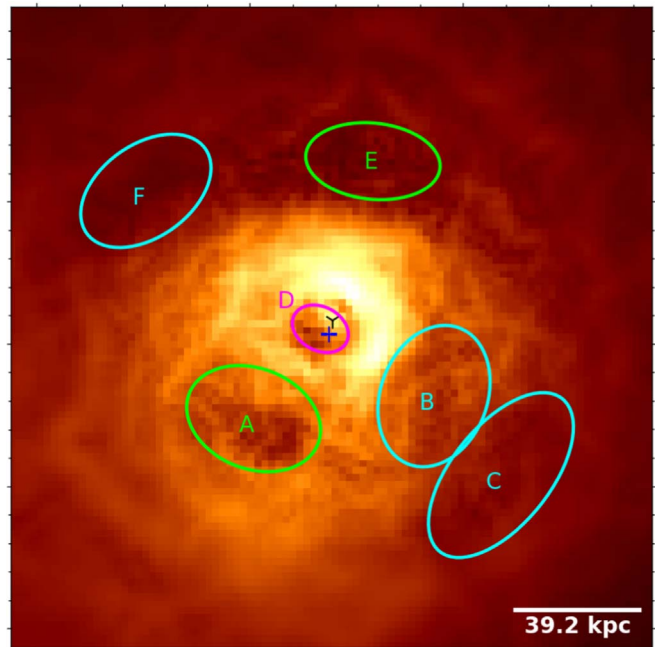
the size of the surface brightness depressions, using the edges identified in the GGM image as a guide. The cavities are shown and labeled in Figure 8. Two cavities were previously reported by Rafferty et al. (2006), though their work used a shallower X-ray image. Judging from the radial distances and sizes of these cavities, one corresponds directly to Cavity "A." The

Table 2
Cavity Measurements

Cavity	FOM[a]	Major (kpc)	Minor (kpc)	R (kpc)	$4pV$ (10^{58} erg)	t_{c_s} (Myr)	t_{buoy} (Myr)	P_{cav} (10^{44} erg s^{-1})	M_{acc} ($10^6 M_\odot$)	$\dot{M}_{acc}$ ($M_\odot$ yr^{-1})	M_{disp} ($10^{10} M_\odot$)
A	1	21.1	15.3	41.7	161^{+58}_{-56}	$38^{+3.2}_{-2.5}$	41.2 ± 2.8	$12.4^{+4.6}_{-4.4}$	$9.02^{+3.3}_{-3.1}$	$0.219^{+0.081}_{-0.077}$	2.69 ± 0.85
B	2	22.2	16.3	38.5	214^{+77}_{-74}	$34^{+2.8}_{-2.2}$	36.3 ± 2.4	$18.7^{+6.9}_{-6.6}$	$12^{+4.3}_{-4.2}$	0.33 ± 0.12	3.35 ± 1.1
C	2	30	15.2	70	204^{+86}_{-68}	$57.5^{+3.2}_{-2.6}$	$71.2^{+4.4}_{-4.3}$	$9.08^{+3.9}_{-3.1}$	$11.4^{+4.8}_{-3.8}$	$0.16^{+0.068}_{-0.054}$	$2.76^{+1.1}_{-0.88}$
D	1	9.01	6.72	7.65	30.6 ± 11	$8.81^{+0.7}_{-0.59}$	$6.68^{+0.62}_{-0.6}$	$14.5^{+5.5}_{-5.3}$	$1.71^{+0.63}_{-0.61}$	$0.257^{+0.097}_{-0.094}$	0.815 ± 0.26
E	3	20.6	11.7	47.5	86.6^{+31}_{-29}	$45.2^{+2.9}_{-2.3}$	52.1 ± 3.3	$5.27^{+1.9}_{-1.8}$	$4.85^{+1.7}_{-1.6}$	$0.0931^{+0.034}_{-0.032}$	$1.58^{+0.52}_{-0.5}$
F	3	22.3	14.2	70	118^{+40}_{-39}	$57.5^{+3.2}_{-2.6}$	$77.9^{+4.8}_{-4.7}$	4.8 ± 1.6	6.61 ± 2.2	0.0847 ± 0.029	1.6 ± 0.51

Note.

[a] The cavity figure of merit, which is a qualitative measure of the contrast between a cavity and its surroundings: (1) high contrast, bright rim surrounds cavity; (2) medium contrast, bright rim partially surrounds cavity; and (3) low contrast, no rim, or faint rim surrounds cavity.

other cavity reported by Rafferty et al. is identified as two in our work—"B" and "C." Cavity "D" is located close to the cluster center and may correspond to motions unrelated to AGN activity, but we tabulate its derived properties nonetheless. Cavities "E" and "F" are located outside of a cold front and are less well defined than their counterparts.

A list of all cavity parameters can be found in Table 2. A qualitative figure of merit (FOM), which describes a cavity's contrast with its surroundings, was provided for each cavity (Rafferty et al. 2006). High contrast cavities (FOM = 1) are surrounded by bright rims, medium contrast (FOM = 2) are partially surrounded by bright rims, and low contrast (FOM = 3) have no or faint rims. All necessary thermodynamic quantities were obtained by interpolating the deprojected radial profiles from Pulido et al. (2018). Note that the proximity of cavity D to the cluster center has a strong systematic effect on the cavity age, and therefore on its power. The cluster centroid was determined from an aperture with a $20''$ (87 kpc) radius. It is offset from the X-ray peak by 6 kpc.

The enthalpy required to inflate a cavity filled with relativistic gas is given by $E_{cav} = 4pV$, where p is the cavity pressure and V is its volume. The cavity was assumed to be in pressure balance with the surrounding gas. The confining pressure was interpolated from the deprojected pressure profile to a radius equal to the distance to the cavity center (R).

The cavity volume was estimated as the geometric mean of the volumes of oblate and prolate geometries, with semiaxes a and b matching those of the fitted ellipse, so that $V = \frac{4}{3}\pi(ab)^{3/2}$. This is equivalent to assuming that the length of the semiaxis along the line of sight is $r = \sqrt{ab}$. The uncertainty for each cavity volume was determined in two ways. First, a 15% uncertainty was assumed in both a and b and propagated. Second, we used the prolate and oblate geometries as measures of the minimum and maximum volumes, respectively. The volume uncertainty was then taken to be the difference between maximum (minimum) volume and cavity volume, in absolute value. This evaluates to a fractional uncertainty of $\sqrt{a/b} - 1$ for an oblate geometry and $1 - \sqrt{b/a}$ for prolate, which are, respectively, the positive and negative errors. This is the dominant uncertainty when $a/b \geqslant 1.74$ when compared to a 15% uncertainty in both a and b.

The cavity age was estimated using both the sound crossing time and buoyant rise time (Bîrzan et al. 2004). The sound crossing time, which assumes the cavity rises at the speed of sound (c_s), is simply a function of ICM temperature, and is

given by

$$t_{c_s} = R/c_s = R\sqrt{\mu m_H / \gamma kT}, \qquad (2)$$

where $\gamma = 5/3$ is the ratio of specific heats for an ideal gas, and $\mu = 0.6$ is the mean particle weight for the ICM. The buoyant rise time is the time taken for the cavity to rise to its current projected distance at its terminal velocity (v_t),

$$t_{buoy} = R/v_t \simeq R\sqrt{SC/2gV}. \qquad (3)$$

Here $C = 0.75$ is the drag coefficient (Churazov et al. 2001) and S is the bubble cross section, which is assumed to be its projected area. The acceleration under gravity at radius R was determined using the cluster mass profile from Pulido et al. (2018). The two timescales agree to within 20% for all cavities. The buoyancy time was used to determine the mean cavity power, $P_{cav} = E_{cav}/t_{buoy}$.

These quantities were then used to place mass constraints on the AGN outbursts. The first, $M_{acc} = E_{cav}/\epsilon c^2$, is the mass that must be accreted onto the black hole to fuel the outburst at an efficiency of ϵ, which we assume to be 0.1. The total accreted gas mass of $4.6 \times 10^7 M_\odot$ can easily be supplied by the observed $5 \times 10^{10} M_\odot$ of molecular gas. The corresponding accretion rate, $\dot{M}_{acc} = P_{cav}/\epsilon c^2$, ranges from ~ 0.1–$0.3 M_\odot$ yr^{-1} for each cavity. The other interesting mass is that of hot gas displaced by the cavities, as this mass dictates the maximum mass that can be lifted by the cavities. The mass of displaced gas is given by $M_{disp} = n\mu m_H V$, where $n = n_e + n_H$ is the density of the surrounding gas. Each of the three larger cavities can lift a few $10^{10} M_\odot$, so the observed molecular gas supply could have been lifted by the cavities.

4. Discussion

4.1. Origin of the Molecular Gas–AGN Offset

As discussed in Section 3.4, the molecular gas and continuum source are mutually offset. The molecular gas resides at the galactic center, while the continuum source is located 2.6 kpc to the NW. In this section we discuss potential causes for this offset. The first two attribute the continuum emission to a source other than the SMBH of the BCG, namely emission from a single lobe of a radio jet or the nucleus of a secondary galaxy. The latter two—gravitational wave recoil and acceleration by an asymmetric radio jet—are mechanisms that would naturally kick or accelerate the black hole from the galactic center.

Offsets between SMBHs and their galactic centers have been observed in other systems (see Bartlett et al. 2020 for an extensive list). Most common are the ∼10–100 pc displacements, which are consistent with an oscillating SMBH following a gravitational wave recoil (e.g., Lena et al. 2014). M87 is an example of such a system, as its SMBH is offset from the photocenter by 6.8 pc (Batcheldor et al. 2010). More exceptional displacements are also observed. The radio-loud quasar 3C 186, for example, harbors an 11 kpc displacement with a corresponding velocity of $-2170\,\mathrm{km\,s^{-1}}$ (Chiaberge et al. 2017).

4.1.1. Emission from a Lobe

Instead of originating from the supermassive black hole's accretion disk, the detected continuum emission could instead originate from the lobe of a radio jet. This would naturally explain the offset, although it requires that the emission from both the core and a second lobe are undetected. Given the rms in the continuum image of $7.5\,\mu\mathrm{Jy\,beam^{-1}}$, any source brighter than $22.5\,\mu\mathrm{Jy}$ would be detected in our observations.

The continuum emission, with a spectral index of 0.7, is consistent with having an origin in an AGN. Spectral indices steeper than 0.5 are generally associated with non-cores, which include lobes, minihalos, and relics (Hogan et al. 2015). If the continuum emission arises from a radio lobe, then it is poorly associated with the X-ray cavities. The continuum emission that would correspond to the putative lobe is located NW of the galactic center, while the most prominent cavities are either to the SE or SW. Cavity D is coincident with the continuum emission, although its overlap with the galactic center makes it difficult to interpret the direction in which the jet would have been launched.

4.1.2. The SMBH of a Secondary Galaxy

The spatially offset continuum emission could also originate from the SMBH in a secondary galaxy that is projected near the BCG core. This SMBH could either be in an independent background galaxy or the center of a galaxy merging with the BCG.

The probability that the continuum source is a chance alignment with an unrelated background radio source is low, based on our estimates of the source density of radio continuum sources at 100 GHz. Lacking a 100 GHz survey sensitive enough to detect the source density down to 0.13 mJy, we have instead used a 31 GHz survey of known extragalactic sources (Mason et al. 2009). A source density of $16.7\,\mathrm{deg^{-2}}$ is appropriate for sources with flux densities $\geqslant 1$ mJy at 31 GHz, which translates to a flux of 0.6 mJy at 100 GHz, assuming a spectral index of 0.4 (Marriage et al. 2011). We then randomly populated 1000 fields each with a source density of $16.7\,\mathrm{deg^{-2}}$. This exercise results in a probability of 1.2×10^{-6} that two sources are separated by $<0''6$. While our assumed density is based on a flux limit of 1 mJy, which is higher than the Zw 3146 continuum source flux (0.133 mJy), the actual source density would need to be several orders of magnitude larger to exceed a probability of close but random coincidence of even a few percent.

The likelihood that the continuum source originates from the core of a merger remnant is much higher. Clumps and trails possibly corresponding to stellar emission from a merger remnant are detected in the HST F606W image (Figure 2). Hβ and [O III] line emission may also contribute to these features. Unlike in systems with dual nuclei, we do not detect excess optical emission at the position of the continuum source. A similar conclusion was drawn in Zw 8193, where the unresolved radio emission is offset from the center of the BCG by $3'$ and may be associated with a merging galaxy (O'Dea et al. 2010).

4.1.3. Gravitational Wave Recoil

As two galaxies merge, their black holes migrate toward the center of the gravitational potential through dynamical friction (Begelman et al. 1980). The resulting binary system tightens through interactions with nearby stars or gravitational drag from gas until the SMBHs eventually coalesce (Merritt & Milosavljević 2005; Mayer et al. 2007). During the final stage of coalescence, the anisotropic emission of gravitational waves imparts a recoil velocity to the coalesced object (González et al. 2007; Campanelli et al. 2007). This "kick" can in rare circumstances be as large as $4000\,\mathrm{km\,s^{-1}}$, and so can result in large displacements between the resulting SMBH and the galactic center.

When an SMBH experiences a large recoil ($v_{\mathrm{kick}} \sim 40$–90% of the escape velocity) in an elliptical galaxy potential, its subsequent motion is characterized by three phases (Gualandris & Merritt 2008). First, the large-scale perturbations—those exceeding the core radius ($r_c \sim 1$ kpc)—are damped within $\sim 10^7$ yr. Then, when the amplitude becomes comparable to the galaxy's core radius, the oscillations of the SMBH persist for ~ 1 Gyr. Finally, the SMBH reaches thermal equilibrium with the stars, at which point the oscillations are negligibly small.

The large (2.6 kpc) displacement observed in Zw 3146 implies that any SMBH coalescence would have occurred recently—within the last 10^7 yr. In a merger between two galaxies with $\sim 10^9\,M_{\odot}$ SMBHs, coalescence occurs within 1–2 Gyr (Khan et al. 2012). Stellar disturbances from a merger will persist for about 2 Gyr (Lotz et al. 2008), but may be shorter lived in a rich cluster. The features observed in the HST F606W image (Figure 2) may correspond to tidal features induced by a merger. Thus, it is plausible that the SMBHs have recently coalesced and that gravitational wave recoil accounts for the displacement of the continuum source.

4.1.4. Acceleration by an Asymmetric Radio Jet

If the radio jets are intrinsically asymmetric in their power output, then the SMBH will experience a net thrust that will displace it from its equilibrium position (Shklovsky 1982). When the black hole is accreting near the Eddington limit, the resulting thrust can cause it to oscillate within the host galaxy (Wang et al. 1992; Tsygan 2007; Kornreich & Lovelace 2008; Lena et al. 2014). Clusters are generally not expected to contain asymmetric jets, as even in the most powerful systems the SMBH resides at the center of the BCG and, on parsec scales, the jets are two sided (Liuzzo et al. 2010). However, while most cavities in Zw 3146 are balanced by another on the opposite side of the BCG, the innermost cavity (cavity D) has no discernible counterpart. Since this cavity is positioned opposite the displacement direction, it can conceivably account for the displacement, provided it was inflated by an asymmetric jet.

The momentum flux for a one-sided relativistic jet is P_{jet}/c. This is the reaction force applied to the black hole from which

the jet originates. The resulting acceleration for a SMBH of mass $M_\bullet$ is

$$a_\bullet = \frac{P_{\text{jet}}}{M_\bullet c} \approx 1.7 \times 10^{-8} \left(\frac{P_{\text{jet}}}{10^{45} \text{ erg s}^{-1}} \right) \left(\frac{M_\bullet}{10^9 M_\odot} \right)^{-1} \text{cm s}^{-2} . \tag{4}$$

The black hole mass in the Zw 3146 BCG, estimated using the 2MASS K-band magnitude, is $M_\bullet = 1.6 \times 10^9 \, M_\odot$ (Main et al. 2017). The black hole acceleration for cavity D, using P_{cav} as an estimate for jet power (see Table 2), evaluates to $1.5 \times 10^{-8} \text{ cm s}^{-2}$.

A displaced black hole will experience a restoring acceleration from the gravitational pull of the BCG. Assuming the BCG is represented by a singular isothermal sphere with velocity dispersion $\sigma_* = 300 \text{ km s}^{-1}$, the gravitational acceleration $(2\sigma^2/R)$ at a displacement of $R = 1 \text{ kpc}$ is $5.8 \times 10^{-7} \text{ cm s}^{-2}$. This is 40 times larger than the acceleration that would be imparted by cavity D assuming that it has no counter-jet. An asymmetric jet can therefore not account for the 2.6 kpc displacement of the continuum source.

4.2. Comparison to Other BCGs

The majority of BCGs contain molecular gas distributions that do not resemble those in gas-rich spiral galaxies. Instead of rotationally supported disks or rings, the cold gas in BCGs is generally filamentary (e.g., Olivares et al. 2019; Russell et al. 2019). In a sample of 12 BCGs, only two have $\leqslant 10\%$ of their total molecular gas located in filaments (Russell et al. 2019). The filaments in the remaining systems account for 30–100% of their molecular gas supplies. These filaments can extend anywhere from several to several tens of kiloparsecs from the galactic center, often in the direction of X-ray cavities (e.g., McNamara et al. 2014; Russell et al. 2016; Vantyghem et al. 2016). Their velocity gradients are often smooth, but are shallower than would be expected from freefall.

The three extensions in Zw 3146 CO(1−0) likely correspond to molecular filaments that are about 4 kpc in length. The outer portions of the filaments, identified by the boxes in Figure 4, account for 40% of the total flux. Radial filaments extending into the galactic center would contain an even larger fraction of the flux. Nevertheless, we are unable to rule out the presence of a molecular disk. The velocity structure, however, is inconsistent with the smooth gradient expected for a disk, so if a disk is present it must be unresolved. Similarly we do not observe the double-horned profile in the CO(1−0) spectrum that is typical of disks.

The system that compares most closely to the Zw 3146 CO(1–0) morphology is PKS0745−191, also at CO(1−0) (Russell et al. 2016). Both exhibit a bright peak near the center of the gas distribution as well as three poorly resolved radial extensions. However, the CO(3–2) observation of PKS0745−191 clearly resolves the three molecular filaments with no significant nuclear structure. The central peak at CO(1−0) results from the coarser resolution blending together the radial filaments. A comparison of Zw 3146 CO(1−0) with both PKS0745−191 CO observations is shown in Figure 9.

Subtracting the central, unresolved emission from the PKS0745−191 CO(1−o) data (see Section 3.2 for the same analysis on Zw 3146), 52% of the total flux can be attributed to an unresolved clump at the peak emission position. This is larger than the 22% measured for Zw 3146 CO(1−0), while in PKS0745−191 CO(3−2) < 5% of the emission is located at the vertex of its three filaments. Without additional higher resolution observations of Zw 3146 we cannot conclusively determine its true molecular gas morphology. However, the similarities with PKS0745−191 suggest that it could share the morphology of three radial filaments with little central emission, observed with intermediate resolution.

4.3. Origin of the Molecular Gas

The massive ($5 \times 10^{10} \, M_\odot$) reservoir of cold gas residing in the central 4 kpc of the Zw 3146 BCG places stringent requirements on its origin. Several tens of gas-rich spiral galaxies would need to be stripped to account for this gas supply. In cluster cores these are rare, as most central galaxies are red, gas-poor ellipticals (Best et al. 2007). Sustained stellar mass loss will contribute to the molecular gas supply, but cannot account for the entire reservoir (Sparks et al. 1989; Voit & Donahue 2011). Instead, like most BCGs, the primary mechanism for forming the molecular gas is the condensation of the hot atmosphere.

Although the hot atmosphere contains ample fuel to produce the molecular gas reservoir, the region covered by molecular emission is dominated by molecular gas. Only $2.5 \pm 0.2 \times 10^{10} \, M_\odot$ of hot gas is present within the central 10 kpc, while the $5 \times 10^{10} \, M_\odot$ of cold gas is located in the central 4 kpc. Zw 3146 is not unique in this regard. In other systems observed by ALMA, the molecular gas mass is approximately equal to the hot gas mass when considering only the region that contains molecular emission (Russell et al. 2019). Forming all of the molecular gas in this region would result in a significant inflow as the central hot atmosphere is depleted. Alternatively, the cold gas could be formed on larger scales in filaments that are too faint to be detected. The Lyα emission, which could be coincident with this fainter molecular line emission, extends well beyond the inner 4 kpc in which the molecular gas is confined. Gas condensing out of the central 20 kpc would have $2 \times 10^{11} \, M_\odot$ of hot gas to draw from.

In the stimulated feedback paradigm, molecular gas condenses from intracluster gas that has been entrained and uplifted by a radio bubble (McNamara et al. 2016). Zw 3146 harbors multiple X-ray cavities that have likely arisen from 2–3 cycles of AGN activity. All three molecular extensions are projected behind an X-ray cavity. The SE and W extensions trail the two most prominent cavities—A and B, respectively. The NE extension trails the most distant and poorly defined cavity (F).

By Archimedes' principle, the maximum mass of gas that can be uplifted in the wake of a rising bubble is given by the mass it has displaced. This demand is alleviated by a factor of a few because the hot atmosphere is initially buoyantly neutral, making the gas easier to lift (Su et al. 2017). The cavities that are associated with a molecular extension have each displaced several $10^{10} \, M_\odot$ of hot gas (see Table 2). This is several times larger than the mass of the molecular gas in the extensions (Table 1). Combined, the cavities displace a total of $1.3 \times 10^{11} \, M_\odot$ of hot gas. Therefore, these cavities could have initiated the formation of the entire $5 \times 10^{10} \, M_\odot$ reservoir of cold gas.

Spectroscopic estimates of the mass deposition rate made using Chandra suggest that the hot atmosphere is condensing at a rate of $300 \, M_\odot \text{ yr}^{-1}$ (Egami et al. 2006b). However, a recent spectral analysis conducted using archival data from the
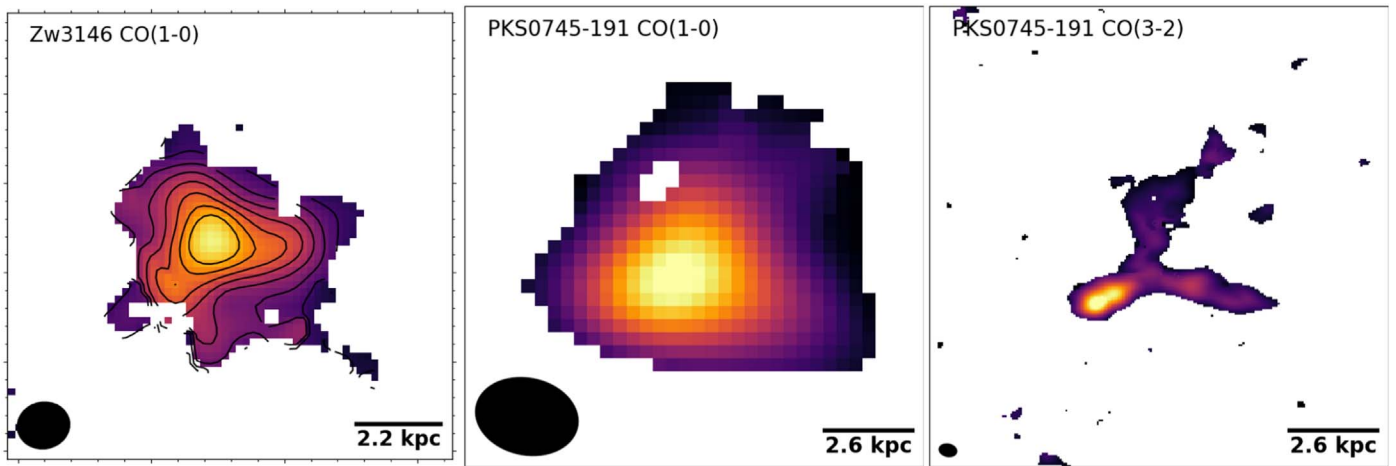
Figure 9. Comparison between total integrated flux maps for Zw3146 CO(1−0) with PKS0745–191 CO(1−0) and CO(3–2).

XMM-Newton Reflection Grating Spectrometer, following the prescription of Liu et al. (2019), measured $<50\,M_\odot\,\mathrm{yr}^{-1}$ of continuous radiative cooling from the bulk temperature (4 keV) down to 0.01 keV (H. Liu et al. 2021, in preparation). This includes $130 \pm 60\,M_\odot\,\mathrm{yr}^{-1}$ of gas cooling to 0.7 keV, with $<78\,M_\odot\,\mathrm{yr}^{-1}$ cooling below that. This is closely matched to the star formation rate of $70 \pm 14\,M_\odot\,\mathrm{yr}^{-1}$.

It would take 1 Gyr to produce the observed reservoir with condensation proceeding at $50\,M_\odot\,\mathrm{yr}^{-1}$. Condensation at this rate over the age of a single cavity would contribute a few times $10^9\,M_\odot$ of cold gas. The ages of the two most energetic AGN outbursts, determined by the buoyancy time of their respective cavities, are $\sim 4 \times 10^7\,\mathrm{yr}$ and $\sim 7 \times 10^7\,\mathrm{yr}$. This translates to the formation of $2 - 3.5 \times 10^9\,M_\odot$ of molecular gas, 4%–7% of the total supply.

Stimulated feedback can therefore contribute significantly to the reservoir of molecular gas, but many cycles of AGN feedback would be required to account for the entire reservoir. Each cycle of AGN feedback can stimulate the formation of a few times $10^9\,M_\odot$ of molecular gas. This process must be sustained for 1 Gyr or longer in order to accumulate the cold gas mass that is observed. The consumption of cold gas in star formation complicates this picture, however, as the star formation rate is comparable to the mass deposition rate.

5. Conclusions

Our ALMA CO(1−0) observations of the Zw 3146 BCG have revealed a massive $(5 \times 10^{10}\,M_\odot)$ reservoir of molecular gas located within 4 kpc of the galactic center. The gas distribution is marginally resolved into three filaments. We have also identified six cavities in the Chandra X-ray image. Each molecular filament trails one of the X-ray cavities.

The cavities have displaced a mass of intracluster gas several times larger than the molecular gas mass, suggesting that stimulated cooling—where low-entropy gas from the cluster core is uplifted by rising radio bubbles until it becomes thermally unstable and condenses—may be responsible for the formation of the molecular gas. However, stimulated cooling would have difficulty accounting for the entire reservoir, as the cavity ages are more than ten times shorter than the 1 Gyr it would take to form $5 \times 10^{10}\,M_\odot$ of cold gas at the observed condensation rate. The total gas supply is likely accumulated over many cycles of AGN feedback, with each cycle shaping its distribution.

While the molecular gas is centered within the BCG, the continuum source originating from the AGN is not. The continuum source is located 2.6 kpc away from the peak of the CO(1−0) emission, placing it at the outer extent of the molecular filaments. The displacement between the continuum source and the galactic center was likely caused by a merger. Possible tidal features within the BCG may be indicative of a merger remnant. The continuum source may correspond to the nucleus of this secondary galaxy. Alternatively, a gravitational wave recoil following a recent $(<10^7\,\mathrm{yr})$ black hole merger may account for this displacement. Alternative mechanisms— such as a chance alignment with a background galaxy, the continuum corresponding to the lobe of a jet, or an asymmetric jet accelerating the SMBH of the BCG—are unlikely.

ORCID iDs

A. N. Vantyghem https://orcid.org/0000-0003-4227-4838
B. R. McNamara https://orcid.org/0000-0002-2622-2627
C. P. O'Dea https://orcid.org/0000-0001-6421-054X
F. Combes https://orcid.org/0000-0003-2658-7893
A. C. Edge https://orcid.org/0000-0002-3398-6916
A. C. Fabian https://orcid.org/0000-0002-9378-4072
M. McDonald https://orcid.org/0000-0001-5226-8349
P. E. J. Nulsen https://orcid.org/0000-0003-0297-4493

References

Alatalo, K., Blitz, L., Young, L. M., et al. 2011, ApJ, 735, 88
Allen, S. W., Edge, A. C., Fabian, A. C., et al. 1992, MNRAS, 259, 67
Bartlett, D. J., Desmond, H., Devriendt, J., Ferreira, P. G., & Slyz, A. 2020, MNRAS, 500, 4639
Batcheldor, D., Robinson, A., Axon, D. J., Perlman, E. S., & Merritt, D. 2010, ApJL, 717, L6
Bayet, E., Hartquist, T. W., Viti, S., Williams, D. A., & Bell, T. A. 2010, A&A, 521, A16
Begelman, M. C., Blandford, R. D., & Rees, M. J. 1980, Natur, 287, 307
Best, P. N., von der Linden, A., Kauffmann, G., Heckman, T. M., & Kaiser, C. R. 2007, MNRAS, 379, 894
Bîrzan, L., Rafferty, D. A., McNamara, B. R., Wise, M. W., & Nulsen, P. E. J. 2004, ApJ, 607, 800
Bîrzan, L., Rafferty, D. A., Nulsen, P. E. J., et al. 2012, MNRAS, 427, 3468
Blanton, E. L., Sarazin, C. L., McNamara, B. R., & Wise, M. W. 2001, ApJL, 558, L15
Böhringer, H., Voges, W., Huchra, J. P., et al. 2000, ApJS, 129, 435
Bolatto, A. D., Wolfire, M., & Leroy, A. K. 2013, ARA&A, 51, 207
Burns, J. O. 1990, AJ, 99, 14
Campanelli, M., Lousto, C. O., Zlochower, Y., & Merritt, D. 2007, PhRvL, 98, 231102
Cavagnolo, K. W., Donahue, M., Voit, G. M., & Sun, M. 2008, ApJL, 683, L107
Chiaberge, M., Ely, J. C., Meyer, E. T., et al. 2017, A&A, 600, A57
Churazov, E., Brüggen, M., Kaiser, C. R., Böhringer, H., & Forman, W. 2001, ApJ, 554, 261
Churazov, E., Forman, W., Jones, C., & Böhringer, H. 2000, A&A, 356, 788
Coble, K., Bonamente, M., Carlstrom, J. E., et al. 2007, AJ, 134, 897
Cowie, L. L., Hu, E. M., Jenkins, E. B., & York, D. G. 1983, ApJ, 272, 29
Crawford, C. S., Allen, S. W., Ebeling, H., Edge, A. C., & Fabian, A. C. 1999, MNRAS, 306, 857
Dasyra, K. M., & Combes, F. 2011, A&A, 533, L10
David, L. P., Lim, J., Forman, W., et al. 2014, ApJ, 792, 94
De Grandi, S., Ettori, S., Longhetti, M., & Molendi, S. 2004, A&A, 419, 7
De Grandi, S., & Molendi, S. 2001, ApJ, 551, 153
Donahue, M., Connor, T., Fogarty, K., et al. 2015, ApJ, 805, 177
Donahue, M., de Messières, G. E., O'Connell, R. W., et al. 2011, ApJ, 732, 40
Dunn, R. J. H., & Fabian, A. C. 2006, MNRAS, 373, 959
Ebeling, H., Edge, A. C., Bohringer, H., et al. 1998, MNRAS, 301, 881
Edge, A. C. 2001, MNRAS, 328, 762
Edge, A. C., Fabian, A. C., Allen, S. W., et al. 1994, MNRAS, 270, L1
Edge, A. C., & Frayer, D. T. 2003, ApJL, 594, L13
Edge, A. C., Oonk, J. B. R., Mittal, R., et al. 2010, A&A, 518, L47
Edge, A. C., Wilman, R. J., Johnstone, R. M., et al. 2002, MNRAS, 337, 49
Egami, E., Misselt, K. A., Rieke, G. H., et al. 2006b, ApJ, 647, 922
Egami, E., Rieke, G. H., Fadda, D., & Hines, D. C. 2006a, ApJL, 652, L21
Fabian, A. C. 1994, ARA&A, 32, 277
Fabian, A. C. 2012, ARA&A, 50, 455
Fabian, A. C., Sanders, J. S., Taylor, G. B., et al. 2006, MNRAS, 366, 417
Ferland, G. J., Fabian, A. C., Hatch, N. A., et al. 2009, MNRAS, 392, 1475
Forman, W., Jones, C., Markevitch, M., Vikhlinin, A., & Churazov, E. 2002, arXiv:astro-ph/0207165
Gaspari, M., Ruszkowski, M., & Oh, S. P. 2013, MNRAS, 432, 3401
Gaspari, M., Temi, P., & Brighenti, F. 2017, MNRAS, 466, 677
Giacintucci, S., Markevitch, M., Venturi, T., et al. 2014, ApJ, 781, 9
González, J. A., Sperhake, U., Brügmann, B., Hannam, M., & Husa, S. 2007, PhRvL, 98, 091101
Gualandris, A., & Merritt, D. 2008, ApJ, 678, 780
Guillard, P., Ogle, P. M., Emonts, B. H. C., et al. 2012, ApJ, 747, 95
Hamer, S. L., Edge, A. C., Swinbank, A. M., et al. 2014, MNRAS, 437, 862
Heckman, T. M. 1981, ApJL, 250, L59
Hicks, A. K., & Mushotzky, R. 2005, ApJL, 635, L9
Hicks, A. K., Mushotzky, R., & Donahue, M. 2010, ApJ, 719, 1844
Hoffer, A. S., Donahue, M., Hicks, A., & Barthelemy, R. S. 2012, ApJS, 199, 23
Hogan, M. T., Edge, A. C., Hlavacek-Larrondo, J., et al. 2015, MNRAS, 453, 1201
Hogan, M. T., McNamara, B. R., Pulido, F., et al. 2017, ApJ, 837, 51
Hu, E. M., Cowie, L. L., & Wang, Z. 1985, ApJS, 59, 447
Kennicutt, R. C., & Evans, N. J. 2012, ARA&A, 50, 531
Kennicutt, R. C., Jr. 1998, ARA&A, 36, 189
Khan, F. M., Preto, M., Berczik, P., et al. 2012, ApJ, 749, 147
Kornreich, D. A., & Lovelace, R. V. E. 2008, ApJ, 681, 104
Lena, D., Robinson, A., Marconi, A., et al. 2014, ApJ, 795, 146

Li, Y., & Bryan, G. L. 2014, ApJ, 789, 54
Lim, J., Ao, Y., & Dinh-V-Trung 2008, ApJ, 672, 252
Lim, J., Ohyama, Y., Chi-Hung, Y., & Dinh-V-Trung, S.-Y. W. 2012, ApJ, 744, 112
Liu, H., Pinto, C., Fabian, A. C., Russell, H. R., & Sanders, J. S. 2019, MNRAS, 485, 1757
Liuzzo, E., Giovannini, G., Giroletti, M., & Taylor, G. B. 2010, A&A, 516, A1
Lotz, J. M., Jonsson, P., Cox, T. J., & Primack, J. R. 2008, MNRAS, 391, 1137
Lynds, R. 1970, ApJL, 159, 10.1086/180500
Main, R. A., McNamara, B. R., Nulsen, P. E. J., Russell, H. R., & Vantyghem, A. N. 2017, MNRAS, 464, 4360
Marriage, T. A., Baptiste Juin, J., Lin, Y.-T., et al. 2011, ApJ, 731, 100
Mason, B. S., Weintraub, L., Sievers, J., et al. 2009, ApJ, 704, 1433
Mayer, L., Kazantzidis, S., Madau, P., et al. 2007, Sci, 316, 1874
McCourt, M., Sharma, P., Quataert, E., & Parrish, I. J. 2012, MNRAS, 419, 3319
McDonald, M., Bayliss, M., Benson, B. A., et al. 2012b, Natur, 488, 349
McDonald, M., Gaspari, M., McNamara, B. R., & Tremblay, G. R. 2018, ApJ, 858, 45
McDonald, M., Veilleux, S., & Rupke, D. S. N. 2012a, ApJ, 746, 153
McDonald, M., Veilleux, S., Rupke, D. S. N., Mushotzky, R., & Reynolds, C. 2011, ApJ, 734, 95
McMullin, J. P., Waters, B., Schiebel, D., Young, W., & Golap, K. 2007, in ASP Conf. Ser., 376, Astronomical Data Analysis Software and Systems XVI, ed. R. A. Shaw, F. Hill, & D. J. Bell (San Francisco, CA: ASP), 127
McNamara, B. R. 2004, in The Riddle of Cooling Flows in Galaxies and Clusters of galaxies, ed. T. Reiprich, J. Kempner, & N. Soker (Charlottesville, VA: Univ. Virginia Press), 177
McNamara, B. R., & Nulsen, P. E. J. 2007, ARA&A, 45, 117
McNamara, B. R., & Nulsen, P. E. J. 2012, NJPh, 14, 055023
McNamara, B. R., Russell, H. R., Nulsen, P. E. J., et al. 2014, ApJ, 785, 44
McNamara, B. R., Russell, H. R., Nulsen, P. E. J., et al. 2016, ApJ, 830, 79
McNamara, B. R., Wise, M., Nulsen, P. E. J., et al. 2000, ApJL, 534, L135
Merritt, D., & Milosavljević, M. 2005, LRR, 8, 8
Morganti, R., Fogasy, J., Paragi, Z., Oosterloo, T., & Orienti, M. 2013, Sci, 341, 1082
Morganti, R., Oosterloo, T., Oonk, J. B. R., Frieswijk, W., & Tadhunter, C. 2015, A&A, 580, A1
Morganti, R., Tadhunter, C. N., & Oosterloo, T. A. 2005, A&A, 444, L9
Nesvadba, N. P. H., Lehnert, M. D., Eisenhauer, F., et al. 2006, ApJ, 650, 693
Nulsen, P., Jones, C., Forman, W., et al. 2009, in AIP Conf. Ser., 1201, The Monster's Fiery Breath: Feedback in Galaxies, Groups, and Clusters, ed. S. Heinz & E. Wilcots (Melville, NY: AIP), 198
O'Dea, C. P., Baum, S. A., Privon, G., et al. 2008, ApJ, 681, 1035
O'Dea, K. P., Quillen, A. C., O'Dea, C. P., et al. 2010, ApJ, 719, 1619
Ogle, P., Boulanger, F., Guillard, P., et al. 2010, ApJ, 724, 1193
Olivares, V., Salome, P., Combes, F., et al. 2019, A&A, 631, A22
Peterson, J. R., & Fabian, A. C. 2006, PhR, 427, 1
Pizzolato, F., & Soker, N. 2005, ApJ, 632, 821
Pizzolato, F., & Soker, N. 2010, MNRAS, 408, 961
Pulido, F. A., McNamara, B. R., Edge, A. C., et al. 2018, ApJ, 853, 177
Rafferty, D. A., McNamara, B. R., & Nulsen, P. E. J. 2008, ApJ, 687, 899
Rafferty, D. A., McNamara, B. R., Nulsen, P. E. J., & Wise, M. W. 2006, ApJ, 652, 216
Revaz, Y., Combes, F., & Salomé, P. 2008, A&A, 477, L33
Rose, T., Edge, A. C., Combes, F., et al. 2019a, MNRAS, 489, 349
Rose, T., Edge, A. C., Combes, F., et al. 2019b, MNRAS, 485, 229
Rose, T., Edge, A. C., Combes, F., et al. 2020, MNRAS, 496, 364
Russell, H. R., McDonald, M., McNamara, B. R., et al. 2017a, ApJ, 836, 130
Russell, H. R., McNamara, B. R., Edge, A. C., et al. 2014, ApJ, 784, 78
Russell, H. R., McNamara, B. R., Fabian, A. C., et al. 2016, MNRAS, 458, 3134
Russell, H. R., McNamara, B. R., Fabian, A. C., et al. 2017b, MNRAS, 472, 4024
Russell, H. R., McNamara, B. R., Fabian, A. C., et al. 2019, MNRAS, 490, 3025
Salomé, P., & Combes, F. 2003, A&A, 412, 657
Salomé, P., Combes, F., Edge, A. C., et al. 2006, A&A, 454, 437
Salomé, P., Combes, F., Revaz, Y., et al. 2008, A&A, 484, 317
Sanders, J. S., Fabian, A. C., Russell, H. R., Walker, S. A., & Blundell, K. M. 2016a, MNRAS, 460, 1898
Sanders, J. S., Fabian, A. C., Taylor, G. B., et al. 2016b, MNRAS, 457, 82
Sharma, P., McCourt, M., Quataert, E., & Parrish, I. J. 2012, MNRAS, 420, 3174
Shklovsky, I. S. 1982, in IAU Symposium, Vol. 97, Extragalactic Radio Sources, ed. D. S. Heeschen & C. M. Wade (Dordrecht: Reidel), 475

Solomon, P. M., Rivolo, A. R., Barrett, J., & Yahil, A. 1987, ApJ, 319, 730
Solomon, P. M., & Vanden Bout, P. A. 2005, ARA&A, 43, 677
Sparks, W. B., Macchetto, F., & Golombek, D. 1989, ApJ, 345, 153
Sturm, E., González-Alfonso, E., Veilleux, S., et al. 2011, ApJL, 733, L16
Su, Y., Nulsen, P. E. J., Kraft, R. P., et al. 2017, ApJ, 847, 94
Tadhunter, C., Morganti, R., Rose, M., Oonk, J. B. R., & Oosterloo, T. 2014, Natur, 511, 440
Tremblay, G. R., Combes, F., Oonk, J. B. R., et al. 2018, ApJ, 865, 13
Tremblay, G. R., O'Dea, C. P., Baum, S. A., et al. 2015, MNRAS, 451, 3768

Tremblay, G. R., Oonk, J. B. R., Combes, F., et al. 2016, Natur, 534, 218
Tsygan, A. I. 2007, ARep, 51, 97
Vantyghem, A. N., McNamara, B. R., Edge, A. C., et al. 2017, ApJ, 848, 101
Vantyghem, A. N., McNamara, B. R., Russell, H. R., et al. 2016, ApJ, 832, 148
Vantyghem, A. N., McNamara, B. R., Russell, H. R., et al. 2018, ApJ, 863, 193
Vantyghem, A. N., McNamara, B. R., Russell, H. R., et al. 2019, ApJ, 870, 57
Voit, G. M. 2018, ApJ, 868, 102
Voit, G. M., & Donahue, M. 2011, ApJL, 738, L24
Wang, J. C. L., Sulkanen, M. E., & Lovelace, R. V. E. 1992, ApJ, 390, 46